Available online at www.sciencedirect.com
SCIENCE DIRECT®
Vision Research 45 (2005) 3189–3201
Vision Research
www.elsevier.com/locate/visres

# Global shape coding for motion-defined radial-frequency contours

Stéphane J.M. Rainville [a,*,1], Hugh R. Wilson [b]

[a] Center for Visual Neuroscience, Department of Psychology, North Dakota State University, Fargo, ND 58105-5075, USA
[b] Center for Vision Research, York University, 4700 Keele Street, North York, Ont., Canada M1J 1P3

Received 4 December 2004; received in revised form 23 June 2005

**Abstract**

The visual system is highly skilled at recovering the shape of complex objects defined exclusively by motion cues. But while low-level and high-level mechanisms involved in shape-from-motion have been studied extensively, intermediate computational stages remain poorly understood. In the present study, we used motion-defined radial-frequency contours—or motion RFs—to probe intermediate stages involved in the computation of motion-defined shape. Motion RFs consisted of a virtual circle of Gabor elements whose carriers drifted at speeds determined by a sinusoidal function of polar angle. Motion RFs elicited vivid percepts of shape, and observers could detect and discriminate radial frequencies up to approximately five cycles. Randomizing Gabor speeds over a small contour segment impaired detection and discrimination performance significantly more than predicted by probability summation. Threshold comparisons between spatial-RF and motion-RF contours ruled out that motion-induced shifts in perceived position (i.e., the DeValois effect) determine shape perception in motion RFs. Together, results indicate that the shape of motion RFs is processed by synergistic mechanisms that perform a global analysis of motion cues over space. These results are integrated with data on perceptual interactions between motion RFs and spatial-RFs [Rainville & Wilson (2004). *Vision Research* 44(11), 1065–1077] and are discussed in terms of cue-specific and cue-invariant representations of object shape in human vision.


*Keywords:* Motion; Form-from-motion; Structure-from-motion; Shape-from-motion

## 1. Introduction

Human vision is highly skilled at recovering the shape of objects defined exclusively by motion cues. Classic examples of shape-from-motion (SFM) include dot displays where no shape is perceived when dots remain static but a vivid percept of shape arises when dots are animated (Gibson, 1986; Johansson, 1973; Todd, 1985; Ullman, 1979; Wallach & O'Connell, 1953). SFM stimuli are inherently ambiguous as the problem of recovering shape-from-motion is mathematically underconstrained and can lead to more than one interpretation. To recover shape-from-motion, the brain must constrain the problem using internal rules and assumptions about the visual environment. The solution that vision has found to the SFM problem is remarkably general, as it operates on a seemingly infinite set of shapes and handles object complexity, non-rigidity, and three-dimensionality with ease. How the brain computes SFM and constrains the solution remains a fundamental issue in visual neuroscience.

Psychophysical studies have relied on two major paradigms—henceforth labelled as the atomistic and holistic approaches—to probe neural mechanisms mediating SFM. The atomistic approach uses basic stimuli such as Gabors (i.e., Gaussian-windowed sinusoidal gratings) to infer the properties of simple mechanisms. These basic stimuli are then combined into more complex stimuli designed to test the rules by which simple mechanisms

* Corresponding author. Tel.: +1 701 231 8625; fax: +1 701 231 8426.
*E-mail address:* rainvill@yorku.ca (S.J.M. Rainville).
[1] Present address: Center for Vision Research, York University, 4700 Keele Street, North York, Ontario, Canada M3J 1P3. Tel.: +1 416 736 2100x33325; fax: +1 416 736 5857.

0042-6989/$ - see front matter © 2005 Elsevier Ltd. All rights reserved.
doi:10.1016/j.visres.2005.06.033

interact and build a representation of motion-defined shape. Atomistic studies have revealed that motion signals are computed locally (Anderson & Burr, 1989; Georgeson & Scott-Samuel, 2000; Qian, Andersen, & Adelson, 1994; Rainville, Scott-Samuel, & Makous, 2002) and pool their outputs to recover local motion speed and direction unambiguously (Adelson & Movshon, 1982; Wilson, Ferrera, & Yo, 1992). Evidence suggests local motion signals interact across space (Loffler & Orbach, 2003; Yuille & Grzywacz, 1988) and serve as input to further stages sensitive to more complex motion properties such as rotation and expansion (Bex & Dakin, 2002; Burr, Morrone, & Vaina, 1998; Lorenceau & Zago, 1999). Atomistic studies also suggest the existence of mechanisms sensitive to motion-defined contours and curvature (Bex, Simmers, & Dakin, 2003; Grzywacz, Watamaniuk, & McKee, 1995; Ledgeway & Hess, 2002; Loffler & Wilson, 2001). The main challenge for the atomistic approach is to probe vision with increasingly complex SFM stimuli whose structure can be represented by models that combine outputs from simple mechanisms in biologically plausible ways.

As an alternative to the atomistic approach, the holistic approach relies on SFM stimuli whose structure is highly complex and/or difficult to describe mathematically, as in the case of natural scenes. These stimuli are then manipulated (or "deconstructed") to probe the properties of visual mechanisms sensitive to SFM. Point-light walkers—stimuli defined only by dots attached to the joints of an animated human figure—are representative of holistic studies on SFM (Johansson, 1973). Even without a complete physical description of their structure, point-light walkers have been used to reveal spatial and temporal integration properties of mechanisms sensitive to biological motion (Giese & Lappe, 2002; Neri, Morrone, & Burr, 1998; Tadin, Lappin, Blake, & Grossman, 2002). The perception of complex motion-defined surfaces and objects has also been explored even if the properties of the retinal image were not fully understood or the stimulus set was too narrowly defined to allow generalization to other stimulus classes (Caudek & Rubin, 2001; Hildreth, Ando, Andersen, & Treue, 1995; Mukai & Watanabe, 1999; Norman & Lappin, 1992; Sperling & Landy, 1989; Watanabe, 1997). Due to the complexity and/or specificity of the stimuli it uses, the holistic approach faces difficulties in modeling and linking results with mechanisms identified by the atomistic approach.

Despite an abundance of data, the visual mechanisms mediating SFM remain poorly understood. Psychophysical data from atomistic and holistic studies are consistent with a visual hierarchy where lower-level signals are selectively combined to represent increasingly complex properties of motion-defined shape (Nakayama, He, & Shimojo, 1995). But while data from the two approaches converge, stimuli remain either too simple or too complex to investigate the processing stages between lower-level and higher-level mechanisms involved in SFM. What is required is a paradigm that investigates intermediate-level stages with a stimulus set that has enough complexity and variety to cover a large space of ecologically valid shapes and yet remains sufficiently simple and well-defined to allow modeling from an atomistic perspective.

In the present study, we investigated intermediate-level SFM using motion-defined radial-frequency stimuli (henceforth referred to as motion RFs). Motion RFs consist of drifting Gabor elements (i.e., sinewaves drifting behind static Gaussian windows) positioned and oriented such as to form a virtual circle (see Fig. 1). While the perceived shape of the stimulus is circular if the stimulus remains static, observers experience a dramatic distortion of the circular shape when Gabors are set in motion—for instance, the circle can be perceived as an ellipse, a square, or other shapes depending on the geometry of the velocity field. Motion RFs have a significant advantage over other SFM stimuli such as point-light walkers: due to the fact that Gabor position is fixed, the shape induced by the Gabor velocity field remains constant and can be studied in its steady state for arbitrarily long stimulus durations.

The geometry of a motion RF's velocity field is typically determined by a single sinusoidal function of polar angle which determines the speed at which each Gabor element is drifting. Through a linear combination of sinusoidal frequencies with appropriate amplitudes and phases (i.e., a Fourier synthesis), the velocity field of motion RFs can perceptually distort circles into single-centroid shapes of arbitrary complexity. The ensemble of motion RFs therefore defines a large and well-parameterized space of motion-defined shapes. The radial-frequency paradigm has been applied successfully to the study of shape perception in the spatial domain with contours defined by position rather than speed (Habak, Wilkinson, Zakher, & Wilson, 2004; Loffler, Wilson, & Wilkinson, 2003; Wilkinson, Wilson, & Habak, 1998) and lends itself well to modeling (Poirier & Wilson, 2004).

Psychophysical experiments reported herein measured the ability of human observers to detect, discriminate, and integrate motion RFs. Results from these experiments show that shape-from-motion is limited to stimuli whose velocity field varies smoothly over space, and that the coding of motion-defined shape is a global process that integrates local motion information synergistically over the extent of the stimulus. Control experiments ruled out the possibility that coding for motion RF exploits illusory positional artefacts reported in studies with drifting Gabor elements (De Valois & De Valois, 1991; Hayes, 2000). Together, results indicate this rich but well-parameterized stimulus set of motion RF contours can successfully probe intermediate-level

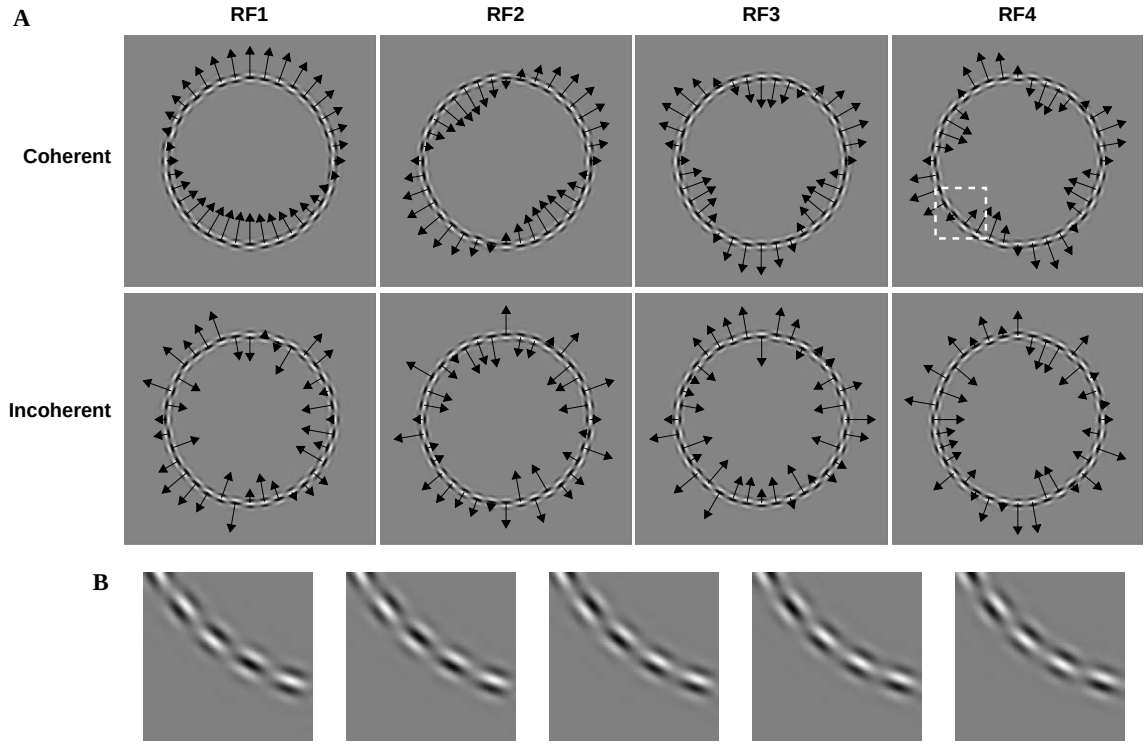


Fig. 1. Motion radial-frequency (RF) contours. (A) Coherent (first row) and incoherent (second row) motion RFs are shown for radial frequencies between 1 and 4 cycles (columns). Coherent motion RFs are composed of 36 Gabor elements drifting at various speeds and directions represented by arrows. Motion-RF amplitude determines global speed and takes values between 0.0 (static) and 1.0 (maximum speed), and motion-RF phase determines the orientation of the sinusoidal modulation in the 2D plane. Incoherent motion RFs are identical to their coherent counterparts with the exception that speeds have been randomly permuted between Gabor elements. Incoherent motion RFs served as comparison stimuli in two-alternative forced-choice detection tasks. Coherent and incoherent motion RFs are indiscriminable in the absence of motion as both stimulus types reduce to a circle of static random-phase Gabors on each frame. (B) Five successive frames that zoom on a square patch (dashed white lines) of the coherent RF4 stimulus in panel (A). These frames emphasize that motion RF structure is defined exclusively by the motion of sinusoidal carriers that drift behind static Gaussian apertures.

SFM processing stages and offers the prospect of a computational account that bridges lower-level and higher-level representations of motion-defined shape.

## 2. Method

### 2.1. Observers

The first author (SR) and three naive observers (BZ, CH, and FP) participated in the study. All observers had normal or corrected-to-normal vision.

### 2.2. Hardware and calibration

Experiments were carried out on an iMac hosting a standard 8-bit/gun color video card driving a built-in 15-in. CRT monitor with a linearized grayscale look-up table of 151 entries. Spatial resolution was set to $640 \times 480$ pixels and the display was run at a refresh rate of 120 Hz. After calibration, the display had a mean luminance of 46.0 cd/m$^2$. Stimuli were generated in the Matlab 5.2.1 environment and displayed using software from the Psychophysics Toolbox (Brainard, 1997) calling lower-level routines from the VideoToobox (Pelli, 1997).

### 2.3. Stimuli and procedure

The geometry of motion RFs is best described in polar coordinates and consists of two components: (1) a *spatial* contour defined by the *position* of co-circular Gabor elements arranged in a circle whose radius determines the absolute dimensions of the stimulus, and (2) a *motion* contour (i.e., a velocity field) defined by the *speed* at which the carrier of each Gabor is drifting behind its static Gaussian aperture (see Fig. 1). Motion contours are specified by a sinusoidal function of polar angle whereby frequency determines the basic shape, amplitude controls deviation from circularity, and phase sets the shape's orientation in the *xy* plane. Examples of basic motion RFs with different radial frequencies are shown in the "coherent" panels of Fig. 1A; "incoherent" stimuli are identical to "coherent" stimuli with the exception that speeds have been randomly permuted between Gabor elements. Random permutation of

speeds ensures that coherent and incoherent stimuli have identical local motion statistics and can only be discriminated on the basis of their global structure.

The spatial-contour component of motion RFs constrains the position and orientation of Gabor elements and therefore forces motion contours into a closed-shape configuration that promotes perceptual grouping (Lorenceau & Alais, 2001). However, the spatial contour itself is common to all stimuli in this study and is therefore of little interest as the positions of the Gaussian envelopes remain fixed and yield no further clues about the shape of motion RFs. This is illustrated in Fig. 1B by a zoom on five successive frames of a motion RF contour (Fig. 1A, dashed white lines in the RF4 "coherent" panel): while neighbouring Gabors drift at different speeds, the speed of each element cannot be inferred by the position of its static Gaussian envelope.

The spatial contour was spatially sampled by an array of 36 co-circular Gabor elements positioned at equal polar-angle intervals on a virtual circle with a radius of 1.6° of arc (100 pixels). The angle $\alpha$ of the $i$th element with respect to the stimulus' center is given by

$$\alpha_i = \frac{2\pi n_i}{N}, \quad n = 0, 1, ..., N-1, \tag{1}$$

where $N$ represents the total number of Gabors. Co-circular elements were obtained by aligning each element's orientation with the virtual circle's local tangent. Envelope position as well as carrier orientation and spatial-frequency remained constant.

The velocity field was created by drifting the carrier of Gabor elements at different speeds. The speed of each Gabor element is given by the time-varying function $\phi$ which specifies the instantaneous carrier phase of the $i$th element on the $t$th movie frame as

$$\phi_i(t) = A \cdot \cos(\omega\alpha_i + \beta) \cdot \pi \cdot t/2 + \Delta_i, \quad t = 0, 1, \ldots, T-1, \tag{2}$$

where $A$ defines the sinusoidal modulation's amplitude, $\omega$ specifies its frequency, $\beta$ determines its phase, and $T$ denotes the total number of frames. The value of $A$ can be no greater than 1.0 to respect the quarter-cycle limit on the $\pi \cdot t/2$ term which advances carrier phase by 90° between successive frames. The term $\cos(\omega\alpha_i + \beta)$ evaluates to a constant for each element and ensures that its speed remains constant across time. The value $\Delta_i$ is a random offset between $-\pi$ and $\pi$ that independently sets the initial carrier phase of each element.

The spatiotemporal properties of the $i$th Gabor element $g$ are given by

$$g_i(x,y,t) = \exp\left[-\frac{(x-x_i)^2 + (y-y_i)^2}{2\sigma^2}\right] \cdot \cos[2\pi((x-x_i)\cos\theta_i - (y-y_i)\sin\theta_i) + \phi_i(t)], \tag{3}$$

where $x_i$ and $y_i$ are its Cartesian center coordinates, $\sigma$ is the space constant of the circular Gaussian envelope, $\theta$ is the orientation of the spatial carrier, and $\phi$ is the time-varying function that defines the shape of the motion contour.

Throughout the experiments, RF contours had a radius of 1.67° of arc, and Gabors had a carrier spatial frequency of 7.8 cpd (wavelength of 8 pixels) and a Gaussian space constant of 3.85 min of arc (4 pixels). Each movie frame was presented for two screen refreshes such that the 120 Hz refresh was halved to an effective frame rate of 60 Hz. Carriers drifting at a maximum modulation amplitude of 1.0 reached a speed of 15 Hz or 1.92° of arc per second. Stimuli were scaled to 100% Michelson contrast and were presented for a total of 29 frames, or 483 ms at 60 Hz. To minimize onset and offset transients, the contrast of the display was ramped between 0% and 100% using a Gaussian temporal window with a time constant of 62.5 ms.

Viewing distance was set to 160 cm such that one pixel subtended 1.0 min of arc. Stimulus presentations were separated by a minimum inter-trial interval of 250 ms, and no feedback was provided.

Data were collected for several modulation amplitudes that were randomly chosen across trials. While the total number of amplitude levels and trials varied across conditions and observers, no fewer than 100 trials were included in the computation of every data point. We fitted two-parameter log $x$-cumulative normals to the percent-correct vs. modulation-amplitude data using a maximum-likelihood criterion and estimated thresholds at the 75%-correct performance level. Error bars showing 95% confidence intervals (±2 SD) were computed using a bootstrapping technique (Efron & Tibshirani, 1993) that modeled our data as a binomial random process. We computed 250 samples from this process, fitted each sample separately, and obtained a distribution of threshold values whose standard deviation we used to compute confidence intervals.

## 3. Shape detection and discrimination

The first experiment consisted of a detection task where observers reported the presence of a coherent motion RF in a temporal two-alternative forced-choice (2AFC) paradigm. The null interval contained an incoherent motion RF derived from the stimulus in the test interval, and intervals were randomly interleaved across trials. We manipulated task difficulty by varying motion-RF amplitude.

Fig. 2A shows motion-amplitude thresholds as a function of radial frequency for three observers. Thresholds remained approximately constant for motion RFs in the 1–4 cycles range but rose significantly at higher RFs. Thresholds for observers BZ and CH could not

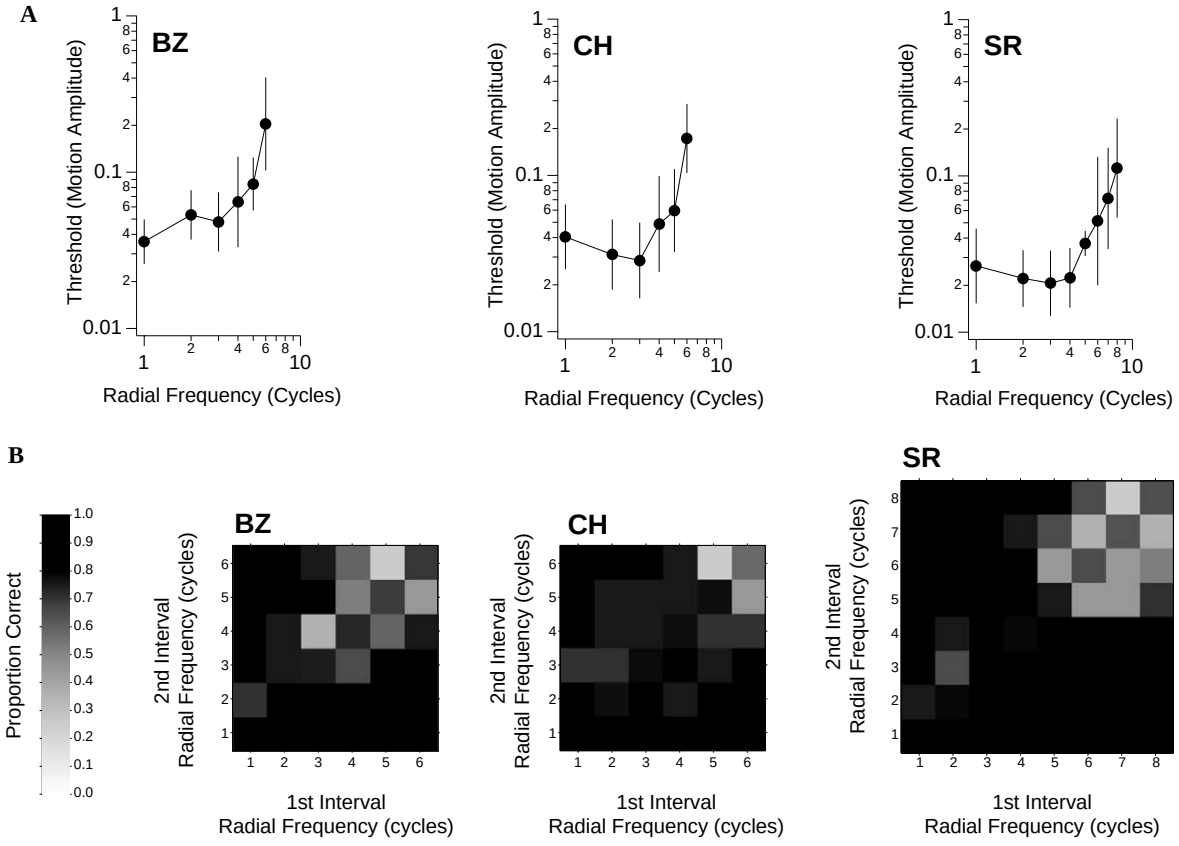


Fig. 2. Detection and discrimination data for motion RFs. (A) Motion-RF detection thresholds as a function of radial frequency. Error bars show 95% confidence intervals (±2 SD). (B) Discrimination performance (proportion correct in a 2AFC) is shown for all possible combinations of radial frequencies and presentation order. Chance performance (0.5) is plotted in gray, and perfect performance (1.0) is plotted in black.

be measured reliably above RF6. Data for motion amplitudes beyond 0.5 were not included in the analysis as observers reported that fast- and slow-moving elements tended to segregate rather than group into a coherent percept.

The second experiment consisted in a two-interval discrimination task where observers made same/different judgements on the radial frequency of pairs of highly visible motion RFs (motion amplitude = 0.25). RF phase was randomized on each interval to ensure observers based on their judgements on stimulus shape rather than local motion cues. The discrimination tasks differs from the detection task in that it requires the *identification* of the motion RF's shape in each interval.

Observers performed same/different judgements for all possible pairwise combinations of the $n$ radial frequencies measured for each observer in the motion RF detection experiment. Because "different" conditions outnumber "same" conditions by a factor of $(n-1)$, we ensured that this asymmetry did not bias observer judgements by presenting an equal number of "same" and "different" trials.

Discrimination data are shown in Fig. 2B where proportion correct is plotted as a function of the radial frequency of the first and second intervals. Chance performance is at 50%, and data confirmed that observers distributed their responses evenly between "same" and "different" conditions. Observers CH and SR easily discriminated between motion RFs in the range of 1–5 cycles whereas motion RFs in the range of 6–8 cycles produced near-chance performance. Observer BZ showed similar results despite some difficulty discriminating between RF3 and RF4. In line with motion RF detection data, results suggest that radial-frequency structure cannot be reliably discriminated beyond approximately five cycles.

Another important observation is that thresholds within the range of RF2–RF5 are comparable to those for RF1 because the velocity field of RF1 stimuli closely approximates translation. It is known that spatial summation for translating stimuli occurs over large portions of the visual field and that increases in performance with larger stimuli follow that of an ideal integrator, not that predicted by probability summation (Burr et al., 1998). Given that thresholds remain approximately flat in the range of RF1–RF5, data from the present section suggest that the processing of low-RF velocity fields involves mechanisms sensitive to the global structure of the stimulus.

## 4. Spatial summation

Experiments in the previous section demonstrate that observers are sensitive to motion-RF contours, but it remains unclear at this point whether local motion cues are integrated into a global representation of shape. In this second set of experiments, we adapted a spatial-summation paradigm from the spatial-RF literature (Loffler et al., 2003) and measured thresholds for detecting and discriminating *partial* motion RFs where a variable-length segment of the coherent motion contour was replaced by an incoherent segment of the same length (see Fig. 3A). Observers discriminated between incoherent contours and partial coherent contours. The rationale for this manipulation is that performance on detection and discrimination tasks should suffer comparatively little if the underlying computation relies only on local features such as curvature because these are abundant in coherent contours interrupted by a short incoherent segment. However, if observers rely on global properties such as contour shape to perform the task, then inserting a short incoherent segment should degrade performance considerably.

Whereas the fully coherent motion RFs used in the previous experiments ensured that coherent structure was available at all locations along the contour, partial motion RFs introduce a spatial uncertainty because the location of the incoherent segment was randomized on each presentation (''random'' condition). To guard against the potential effects of this positional uncertainty, we repeated the partial-motion RF experiment and restricted the center of the coherent segment to fall on one of five adjacent Gabors in the top part of the display (''fixed'' condition). Observers in the fixed condition were given a priori knowledge of the coherent segment's location.

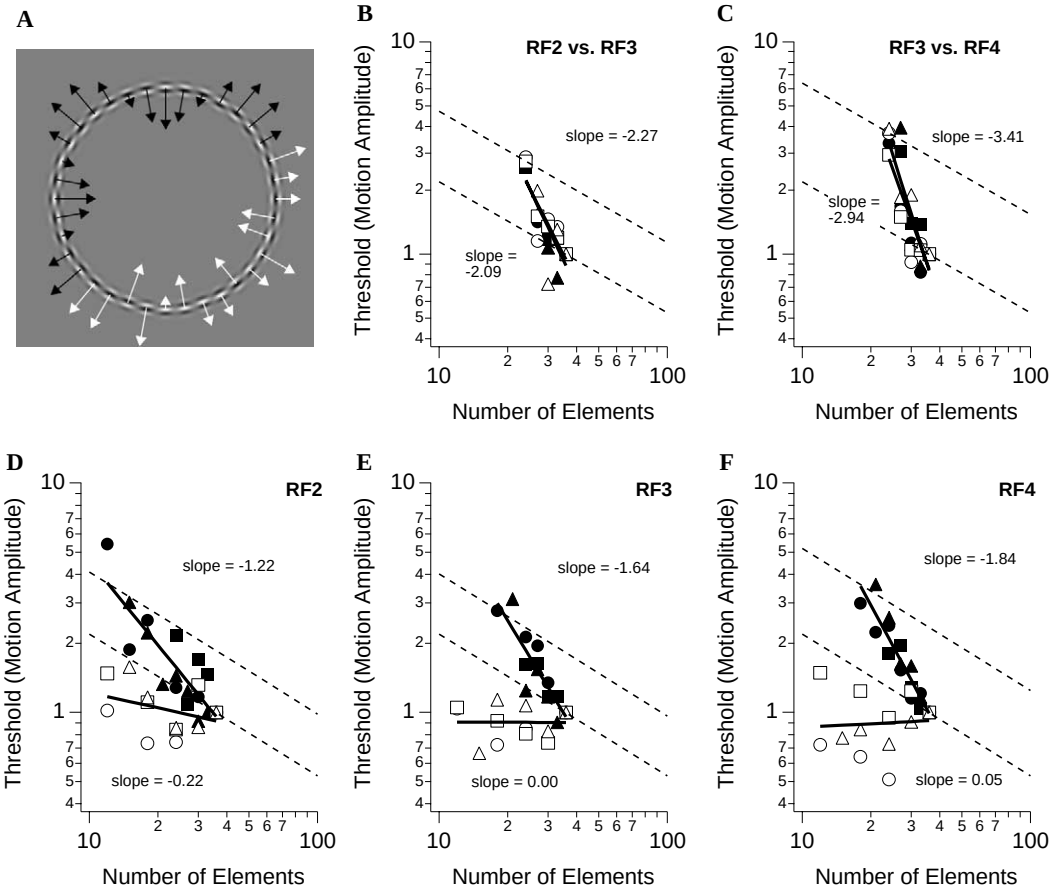


Fig. 3. Detection and discrimination data for partial motion RFs. (A) Example of a partial motion RF4 pattern with coherent (black arrows) and incoherent (white arrows) segments. We varied the length (i.e., the number of elements) of the coherent segment and permuted speeds between remaining elements. In other panels, data are shown from three observers represented by circles, squares, and triangles respectively. Filled and open symbols indicate the ''random'' and ''fixed'' condition where the location of the coherent segment was either unpredictable or known a priori by observers. (B) Threshold-elevation data for discriminating between motion RF2 and motion RF3 patterns as a function of coherent segment length. (C) Same as (B) but for discriminating between RF3 and RF4. (D–F) Threshold-elevation data for detecting RF2, RF3, and RF4 patterns respectively. Data are normalized to unity with respect to the full coherent motion RFs (36 elements) measured in previous experiments. Log-slopes of the best-fitting power-law function to the data are indicated. Dashed lines show the rate of threshold elevation (slope = −0.62) expected from probability summation. Confidence intervals have been omitted for clarity but are comparable to those in Fig. 2A.

Fig. 3 shows threshold-elevation curves for detecting (panels D–F) and discriminating (panels B and C) partial motion RFs. Data for three observers (square, circle, and triangle symbols) are plotted as a function of the length of the coherent segment (i.e., the number of elements that composed the coherent segment). Open and closed symbols correspond to the fixed and random conditions respectively. Solid lines show the best fit of a power-law function to the combined data from all three observers in each condition.

Results from the detection experiment (Figs. 3D–F) show that thresholds in the fixed condition (open symbols) are largely unaffected by the length of the coherent segment. Unlike incoherent contours, coherent contours impose a smoothness constraint across space such that neighbouring elements tend to move in similar directions and have similar speeds. For this reason, results in the fixed detection condition are not unexpected as knowledge of the coherent segment's spatial location allows observers to distinguish between coherent and incoherent motion RFs simply by monitoring direction of motion in a few elements.

In the random detection condition (closed symbols in Figs. 3D–F), detection thresholds decrease as a function of the coherent segment's length. As the location of the coherent contour in the random condition was unpredictable, observers could no longer rely on the simple strategy of monitoring direction of motion in a few elements. Instead, observers in the random condition were likely forced to rely on a less efficient strategy such as monitoring the output of mechanisms sensitive to contour shape.

Results from the discrimination experiment (Figs. 3B and C) differ from those of the detection experiment in that prior knowledge of the coherent segment's position does not improve performance. Whereas considering a few elements is sufficient to distinguish coherent from incoherent motion RFs in the fixed *detection* condition, such a strategy is not successful in the fixed *discrimination* condition because there is little local information that distinguishes two motion contours of different radial frequencies. Discrimination therefore forces observers to compare the global shape of stimuli in the two intervals. The discrimination experiment rules out positional uncertainty as a factor and indicates that even short incoherent segments severely interfere with shape discrimination.

With the exception of the fixed detection condition, all thresholds decrease as a function of coherent contour length at a faster rate than predicted by probability summation (dashed lines). Probability summation corresponds to the improvement in performance expected from the statistical recruitment of independent mechanisms sensitive to local contour information; by comparison, linear summation (slope $= -1.0$) is consistent with linear filtering (e.g., a cross-correlation between a stimulus and a matched template). Slopes steeper than $-1.0$ imply that local information is combined in a synergistic (i.e., non-linear cooperative) fashion across space and are indicative of a high degree of stimulus selectivity from underlying mechanisms. The threshold-elevation curves predicted by probability summation (dashed lines) were calculated on data pooled across all observers and all conditions and fitted with a Quick–Weibull function: the slope of the probability–summation curve (i.e., $-0.62$) corresponds to the negative-log-inverse of the slope of the fitted psychometric function (Graham, 1989; Loffler et al., 2003).

Together, these data constitute some of the strongest evidence for mechanisms that actively compute motion-defined shape through the synergistic pooling of local velocity. We further elaborate on this conclusion in Section 5.

### 4.1. The DeValois effect

De Valois and De Valois (1991) reported that the envelope of a drifting Gabor appears shifted from its veridical position towards the direction of the carrier's motion. A natural question, then, is whether such illusory shifts in Gabor position (rather than Gabor motion per se) are involved in processing motion RFs. To test for this possibility, we used a multi-step approach which we summarize here for clarity before elaborating on each step in paragraphs below. We first measured detection thresholds for *spatial* RFs and *motion* RFs separately (recall that motion RFs are defined by Gabor speed whereas spatial RFs are defined by Gabor position). Detection thresholds were measured in the same way for both types of RFs, namely by varying the amplitude of the underlying sinusoidal component. We then measured the DeValois effect as a function of Gabor speed in Vernier alignment tasks; this provided us with empirical transfer functions for mapping any Gabor speed onto its perceived spatial position. Finally, we computed the effective *spatial* amplitude of *motion* RFs by applying the speed-to-position function to every moving Gabor in the display. As the DeValois effect predicts that motion-RF and spatial-RF thresholds should be identical, any significant discrepancies would indicate shape perception in motion-defined RFs is not mediated by illusory shifts in Gabor position.

In the first step, we measured detection thresholds separately for spatial RFs and motion RFs whose Gabor elements were subjected to variable amounts of positional noise (i.e., random jitter added to the physical position of each Gabor elements along the radial dimension of the stimulus). Examples of spatial-RF and motion-RF stimuli with a moderate level of positional noise are shown in Fig. 4A. The purpose of positional noise was to obtain detection thresholds over a sufficiently large range to reveal discrepancies between spa-

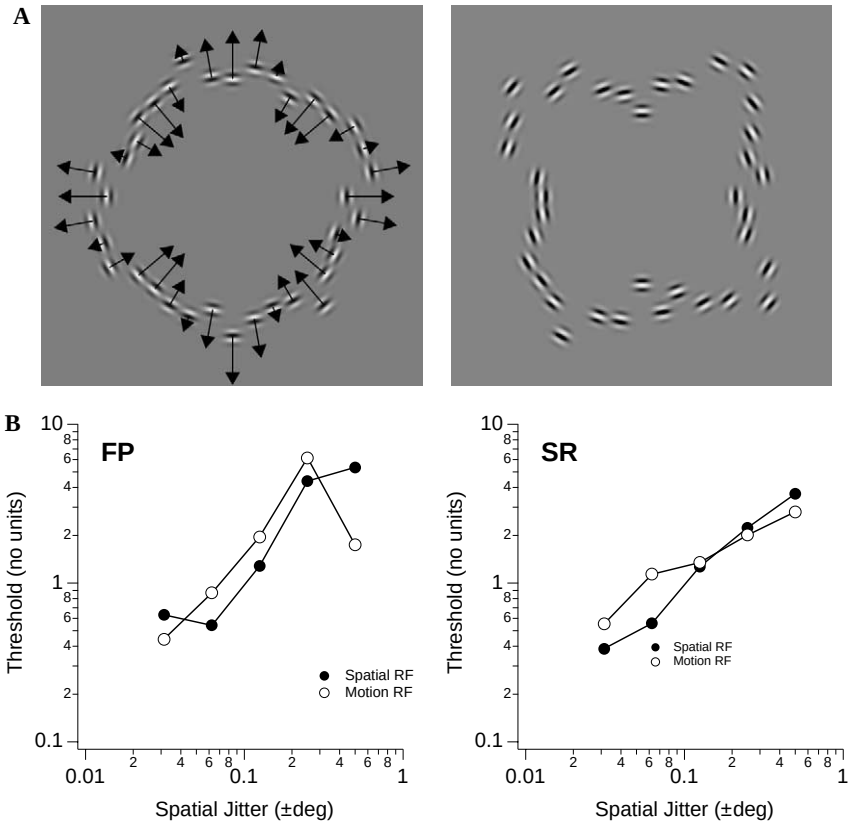


Fig. 4. Motion and spatial RF4s. (A) Examples of a motion RF4 (left) and spatial RF4 (right). Both stimuli are shown here with moderate amounts of random positional jitter applied to each Gabor element. (B) Detection thresholds for motion RFs (open circles) and spatial RFs (closed circles) as a function of positional jitter. Motion RF and spatial RFs data have been normalized into approximately the same logarithmic range in order to emphasize that jitter produces similar threshold slopes in both conditions. Absolute thresholds cannot be compared meaningfully because they do not share a common metric.

tial-RF and motion-RF conditions. Although absolute thresholds for spatial RFs and motion RFs do not share the same metric and therefore cannot be plotted on the same scale, it is possible to compare how thresholds are affected by positional noise. Data for motion RFs and spatial RFs are plotted in Fig. 4B for two observers. Although absolute threshold values are meaningless, results show that positional noise elevates detection thresholds by similar amounts for both stimulus types.

In the second step, we measured the DeValois effect in so-called "local" and "global" conditions. In the local condition, observers performed a single-interval Vernier alignment task and reported whether the perceived position of a *drifting* test appeared shifted to the left or the right of two *static* flankers (see Fig. 5A). The physical position of the test was varied over a range of horizontal offsets, and the direction of drift was selected randomly on each trial to avoid motion after-effects (randomizing motion direction also avoids response biases inherent to single-interval tasks). We measured the motion-induced shift in Gabor position over a range of drift speeds and repeated the experiment at three eccentricities (0°, 1.5°, and 3.0°) as the magnitude of the DeValois effect is known to increase with eccentricity (De Valois & De Valois, 1991). The global condition was similar to the local condition with the exception that observers judged whether the position of a *static* Gabor test fell inside or outside a *motion*-defined circular contour (i.e., motion RF0) undergoing either contraction or expansion. The purpose of the global condition was to cover the possibility that the DeValois effect is somehow amplified by having several Gabor elements undergo coherent motion. An example of the global condition is shown in Fig. 5B. Gabors used to measured the DeValois effects had identical spatial and temporal properties to those in other experiments in this paper.

Perceived shift in Gabor position is plotted as a function of drift speed for the local and global conditions in Figs. 5A and B respectively. Results revealed that the perceived positional shift varies as a sigmoidal function of log-speed and reaches maximum illusory displacements in the range of 0–3 min of arc in the local condition, and between 0 and 5 min of arc in the global condition. We fitted log-cumulative-normals to the data and obtained speed-to-position transfer curves for evaluating illusory positional shifts as a function of drift speed. These experiments produced only modest eccentricity effects due presumably to the relatively high spa-

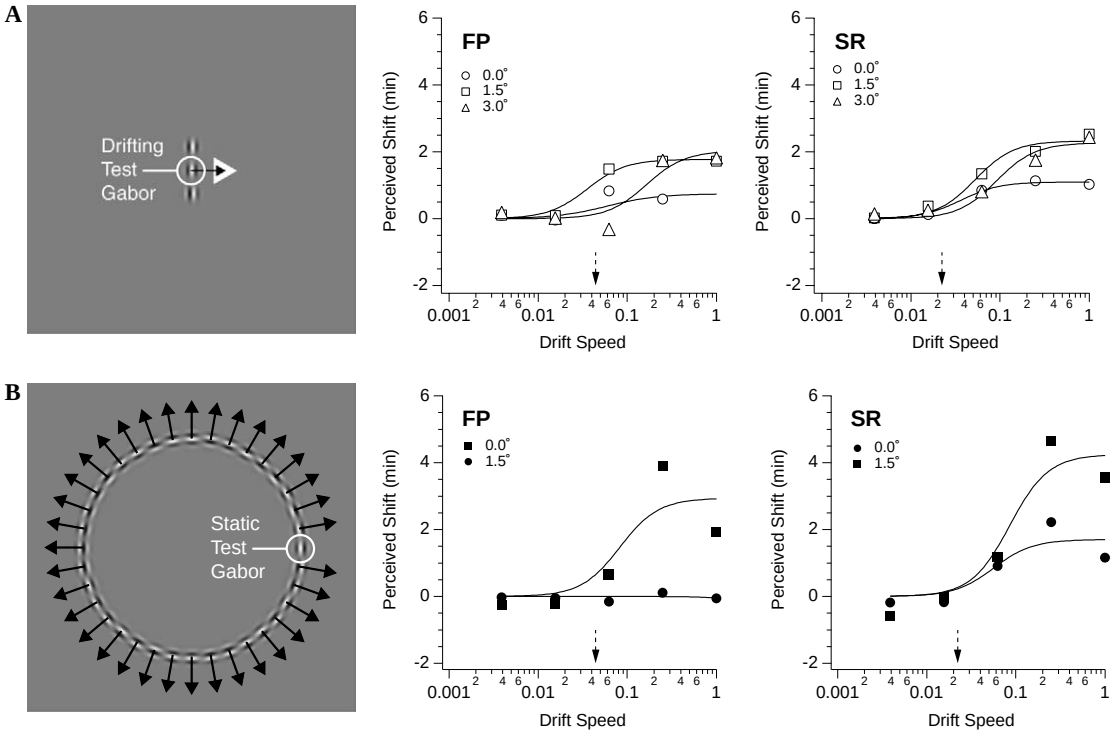


Fig. 5. Measuring the DeValois effect. (A) Local Vernier alignment task where observers aligned the position of a central drifting Gabor test with the position of two static flankers. Perceived positional shift as a function of test speed is shown for two observers and three eccentricities (open symbols). (B) Global Vernier alignment task where observers indicated whether a static test Gabor was perceived as inside or outside a circle of drifting Gabor elements (i.e., Motion RF0). Perceived positional shift as a function of drift speed is shown for two observers and two eccentricities (closed symbols). Arrows on each graph indicate drift speeds corresponding to motion-amplitude thresholds in the absence of spatial jitter.

tial frequency (7.5 cpd) of the Gabor patterns and the correspondingly small range of eccentricities over which the Vernier display was visible. Illusory shifts could be measured reliably up to 3.0° of eccentricity in the local task and up to 1.5° in the global task. These small ranges of eccentricity, combined with the fact that Gabors themselves were virtually invisible beyond approximately 5.0° of arc, imply that observers did not rely on perifoveal or peripheral viewing of the stimuli in experiments reported in the present paper.

In a third and final step, we leveraged the DeValois effect to provide a common metric for absolute motion-RF thresholds and absolute spatial-RF detection thresholds. As detection thresholds for motion RFs completely specify the speed of each Gabor element in the stimulus, we converted the speed of each Gabor element into its positional equivalent via the measured speed-to-position transfer functions (see Fig. 5) and computed the effective spatial-RF amplitude of motion RFs using the best least-squares fit of a sinewave to the transformed stimulus. Absolute spatial-RF thresholds are plotted in Fig. 6 (filled inverted triangles), and absolute motion-RF thresholds predicted by each of the speed-to-transfer functions measured for local and global Vernier tasks at various eccentricities are plotted on the same scale.

Data from Fig. 6 show that spatial-RF thresholds exceed the motion-RF thresholds predicted by the DeValois effect by several orders of magnitude. These data therefore suggest that the perception of motion-RF contours is not mediated by illusory shifts in Gabor position. Data also argue against the possibility of a "synergistic" variant of the DeValois effect where illusory positional shifts might be enhanced when several drifting Gabor elements form a coherent motion contour.

## 5. Discussion

The present study has used motion-defined radial-frequency contours to investigate intermediate-level mechanisms mediating shape-from-motion. A first set of experiments revealed that the detection and discrimination of motion RFs are limited to low-radial frequencies (i.e., velocity fields that vary smoothly over space). A second set of experiments showed that inserting a small incoherent segment in an otherwise coherent motion RF severely disrupts detection and discrimination performance. A third set of experiments examined the potential role of the DeValois effect and found that illusory shifts in Gabor position play no significant role in the

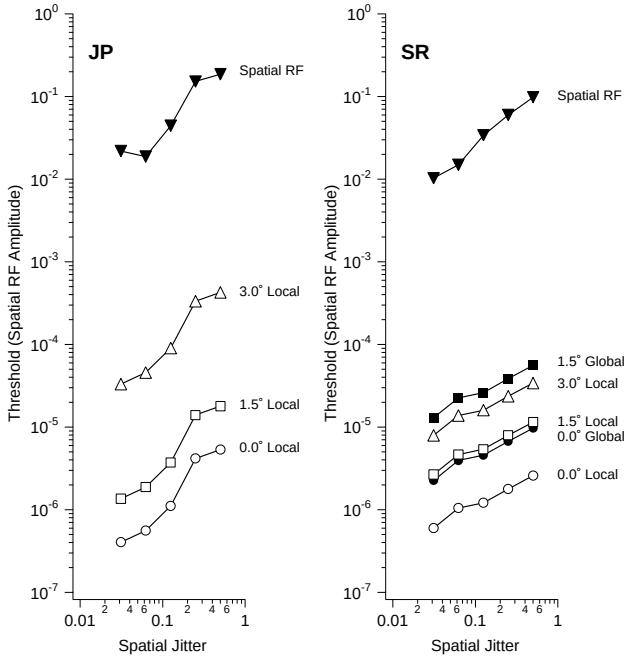


Fig. 6. Comparing motion RFs and spatial RFs via the DeValois effect. Absolute detection thresholds for spatial RF4s and motion RF4s are plotted as a function of spatial jitter for two observers. Thresholds are expressed as in terms of spatial amplitude both for spatial and motion RF4. Whereas spatial-RF thresholds were measured directly, motion-RF thresholds were converted into spatial-RF thresholds via the various DeValois speed-to-position transfer functions shown in Fig. 5. Note that symbols between Fig. 5 and this figure match to simplify comparisons.

perception of shape in motion RFs. Implications of these results are discussed below.

Previous research has shown that object shape and object motion are computed by separate visual streams that project ventrally and dorsally from primary visual cortex (V1) to infero-temporal and posterior-parietal cortex respectively (DeYoe & Van Essen, 1988; Livingstone & Hubel, 1987; Ungerleider & Desimone, 1982). However, this coarse functional distinction between ventral and dorsal pathways is disputed (Braddick, O'Brien, Wattam-Bell, Atkinson, & Turner, 2000). Several cortical areas in the ventral and dorsal streams have been implicated in shape-from-motion (Grossman & Blake, 2002; Kourtzi, Bulthoff, Erb, & Grodd, 2002; Vaina, Solomon, Chowdhury, Sinha, & Belliveau, 2001), and recent imaging data point to a third stream projecting from V1 to lateral occipito-temporal cortex which also underlies complex motion perception (Beauchamp, Lee, Haxby, & Martin, 2003; Grill-Spector, Kushnir, Edelman, Itzchak, & Malach, 1998). Evidence suggests that each stream consists of a hierarchy of processing stages that transform lower-order stimulus properties into higher-order primitives (Gallant, Connor, Rakshit, Lewis, & Van Essen, 1996; Grill-Spector et al., 1998; Tanaka, 1996; Tanaka & Saito, 1989; Wurtz & Duffy, 1992), and anatomical work has revealed reciprocal inter-stream connections at all levels of the visual hierarchy (Felleman & Van Essen, 1991; Van Essen & Maunsell, 1983; Young, 1992).

Given the significant exchange of information between major visual pathways, it is particularly relevant to ask how motion RFs and spatial RFs interact at the neural level. In a previous study, we addressed this issue by superimposing spatial-RF tests on motion-RF masks of identical radial frequency (Rainville & Wilson, 2004). We found that the modulation of a spatial-RF test could be nulled perceptually by adjusting the amplitude of a superimposed motion RF mask of the opposite phase. Results from that study therefore suggest a common stage for processing motion RFs and spatial RFs, and several clues from this study suggested that this common stage did not consist of local low-level interactions that characterize the DeValois effect (De Valois & De Valois, 1991). The present study further rules out the DeValois effect's involvement in motion-RF perception and supports our conclusion that spatial RFs and motion RFs interact, but only through later stages concerned with higher-level stimulus features such as curvature or overall shape.

Spatial-summation experiments from the present study indicate that the integration of motion RF contours operates synergistically over space. Similar results have been obtained with biological motion (Neri et al., 1998), and data from experiments with partial spatial RFs have also demonstrated threshold elevations in excess of probability summation (Loffler et al., 2003). Although performance with spatial RFs did not reach synergistic summation and approached linear summation only at low RFs, differing results between motion and spatial RFs may be attributable to discrepancies between the two stimulus types—for instance, contour segments were replaced by noise in motion RFs but were replaced by purely circular segments in spatial RFs. Whether shape coding is synergistic or quasi-linear, supra-probabilistic summation for spatial and motion RFs implies a global representation of shape at some level in the visual hierarchy. Given that spatial and motion RFs perceptually interact, an important issue is the level in the visual hierarchy at which these two stimulus types share a common representation.

Recent lateral-masking data from our laboratory suggest that the processing of spatial RFs is not mediated by the network of horizontal connections found in V1 (Cavanaugh, Bair, & Movshon, 2002; Das & Gilbert, 1995) which favors straight contours over curved ones (Habak et al., 2004). In line with a previous imaging study (Wilkinson et al., 2000), lateral masking suggests that concentric patterns such as spatial RFs are instead processed by extrastriate in areas such as V4. Interestingly, physiological recordings from monkey V4 have revealed cells selective not only for local curvature but also for the angular position of curved segments along con-

centric contours (Pasupathy & Connor, 2002). The same study demonstrated that a population code consisting of V4 cells can represent the space of curvature vs. angular-position with enough fidelity to recover simple curvilinear shapes.

One scenario, then, is that the shape of spatial RFs and motion RFs are represented by separate mid-level systems whose outputs interact only at the highest stages in the visual hierarchy such as STS (Grossman et al., 2000). Consistent with this idea, physiological data from mid-level areas such as MST involved in motion processing show a sensitivity to radial motion (Duffy, 1998; Duffy & Wurtz, 1991) and to object shape (Kourtzi et al., 2002), although because receptive fields in MST are large (~40°) such mechanisms are perhaps more suitable for computing optic flow than object shape (Loffler & Wilson, 2001). Evidence for mechanisms sensitive to motion-defined curvature is found in psychophysical experiments (Ledgeway & Hess, 2002), and physiological experiments report that MT cells have a columnar organization (Albright, Desimone, & Gross, 1984) with center–surround properties (Gautama & Van Hulle, 2001; Xiao, Raiguel, Marcar, & Orban, 1998) that may be suitable for extracting motion-defined curvature. However, whether motion-sensitive areas such as MT/MST implement a curvature vs. angular-position population code similar to the one V4 uses to process spatial contours (Pasupathy & Connor, 2002) remains an open question.

A second scenario is that motion RFs and spatial RFs share a "cue-invariant" representation of shape at a common mid-level stage in the visual hierarchy such as area V4 or LOC—the lateral occipital complex (Kourtzi & Kanwisher, 2001). In fact recent fMRI data from our laboratory suggest LOC encodes simple spatial shapes in terms of deviations from circular prototypes (Rainville & Wilson, 2005). Physiological studies show a strong connectivity between motion-sensitive area MT and contour-sensitive V4 (Maunsell & van Essen, 1983; Merigan & Maunsell, 1993; Ungerleider & Desimone, 1986; Van Essen, Maunsell, & Bixby, 1981), and the anatomical proximity of LOC with MT and MST favors the interchange of information between motion and shape-sensitive areas (Kourtzi et al., 2002). Thus basic information such as smoothness of a velocity field could be relayed from MT/MST to build a single common (i.e., cue invariant) representation of object shape in V4/LOC. Which of these two scenarios is more likely will require further research on intermediate-level mechanisms mediating the computation of shape in the spatial and motion domains.

Another important question concerns the ecological validity of motion-RF stimuli: spatial RFs can model the outline of naturalistic objects such as faces and fruits, but do motion RFs find an equally valid correspondence in natural scenes? While only a computational study of natural-scene statistics can settle the issue, it is interesting to note that there are at least three important classes of naturally occurring stimuli that produce retinal images with properties similar to motion RFs: (i) looming (e.g., a fast-approaching face), (ii) deforming 2D objects (e.g., a mouth pronouncing words), and (iii) rotating 3D objects (e.g., the outline of a turning head). In all three cases, a concentric velocity field is carrying information about object shape. As we alluded to in previous paragraphs, motion receptive fields with complex properties (e.g., expansion, rotation, spiral basis sets) have been found in cortical areas such as MST and could be part of a network involved in the computation of motion-defined shape.

## 6. Conclusion

Results from the present study have revealed that intermediate-level mechanisms mediating shape from motion are limited to motion-defined contours with velocity fields that vary smoothly over space. Results rule out the simple explanation that shape perception with motion RFs is mediated by spatial mechanisms that exploit illusory motion-induced shifts in position (i.e., the DeValois effect). Data also ruled out that the coding of shape in motion-defined contours is mediated by probability summation over low-level motion cues; instead, as with spatial RFs, results point to active mechanisms that integrate motion-defined contours over space in a synergistic (i.e., non-linearly cooperative) fashion. It remains unclear whether perceptual interactions between spatial-RFs and motion RFs point to a shared (i.e., cue invariant) mid-level representation of shape or whether motion pathways compute shape-from-motion independently and defer pathway interactions to later stages in the visual hierarchy. However, such questions may be answered empirically with stimuli such as radial-frequency contours designed to bridge lower-level and higher-level mechanisms involved in the computation of object shape.

## Acknowledgments

We thank the Natural Sciences and Engineering Research Council of Canada (grant OP227224) and the National Institute of Health (grant EY002158) for their support. We are also grateful to Gunter Löffler for useful discussions and suggestions.

## References

Adelson, E. H., & Movshon, J. A. (1982). Phenomenal coherence of moving visual patterns. *Nature, 300*(5892), 523–525.

Albright, T. D., Desimone, R., & Gross, C. G. (1984). Columnar organization of directionally selective cells in visual area MT of the macaque. *Journal of Neurophysiology, 51*(1), 16–31.

Anderson, S. J., & Burr, D. C. (1989). Receptive field properties of human motion detector units inferred from spatial frequency masking. *Vision Research, 29*(10), 1343–1358.

Beauchamp, M. S., Lee, K. E., Haxby, J. V., & Martin, A. (2003). FMRI responses to video and point-light displays of moving humans and manipulable objects. *Journal of Cognitive Neuroscience, 15*(7), 991–1001.

Bex, P. J., & Dakin, S. C. (2002). Comparison of the spatial-frequency selectivity of local and global motion detectors. *Journal of the Optical Society of America, A, Optics, Image Science, & Vision, 19*(4), 670–677.

Bex, P. J., Simmers, A. J., & Dakin, S. C. (2003). Grouping local directional signals into moving contours. *Vision Research, 43*(20), 2141–2153.

Braddick, O. J., O'Brien, J. M., Wattam-Bell, J., Atkinson, J., & Turner, R. (2000). Form and motion coherence activate independent, but not dorsal/ventral segregated, networks in the human brain. *Current Biology, 10*(12), 731–734.

Brainard, D. H. (1997). The psychophysics toolbox. *Spatial Vision, 10*, 443–446.

Burr, D. C., Morrone, M. C., & Vaina, L. M. (1998). Large receptive fields for optic flow detection in humans. *Vision Research, 38*(12), 1731–1743.

Caudek, C., & Rubin, N. (2001). Segmentation in structure from motion: Modeling and psychophysics. *Vision Research, 41*(21), 2715–2732.

Cavanaugh, J. R., Bair, W., & Movshon, J. A. (2002). Nature and interaction of signals from the receptive field center and surround in macaque V1 neurons. *Journal of Neurophysiology, 88*(5), 2530–2546.

Das, A., & Gilbert, C. D. (1995). Long-range horizontal connections and their role in cortical reorganization revealed by optical recording of cat primary visual cortex. *Nature, 375*(6534), 780–784.

De Valois, R. L., & De Valois, K. K. (1991). Vernier acuity with stationary moving Gabors. *Vision Research, 31*(9), 1619–1626.

DeYoe, E. A., & Van Essen, D. C. (1988). Concurrent processing streams in monkey visual cortex. *Trends in Neurosciences, 11*(5), 219–226.

Duffy, C. J. (1998). MST neurons respond to optic flow and translational movement. *Journal of Neurophysiology, 80*(4), 1816–1827.

Duffy, C. J., & Wurtz, R. H. (1991). Sensitivity of MST neurons to optic flow stimuli. I. A continuum of response selectivity to large-field stimuli. *Journal of Neurophysiology, 65*(6), 1329–1345.

Efron, B., & Tibshirani, R. J. (1993). *An introduction to the bootstrap*. New York: Chapman & Hall.

Felleman, D. J., & Van Essen, D. C. (1991). Distributed hierarchical processing in the primate cerebral cortex. *Cerebral Cortex, 1*(1), 1–47.

Gallant, J. L., Connor, C. E., Rakshit, S., Lewis, J. W., & Van Essen, D. C. (1996). Neural responses to polar, hyperbolic, and Cartesian gratings in area V4 of the macaque monkey. *Journal of Neurophysiology, 76*(4), 2718–2739.

Gautama, T., & Van Hulle, M. M. (2001). Function of center–surround antagonism for motion in visual area MT/V5: A modeling study. *Vision Research, 41*(28), 3917–3930.

Georgeson, M. A., & Scott-Samuel, N. E. (2000). Spatial resolution and receptive field height of motion sensors in human vision. *Vision Research, 40*(7), 745–758.

Gibson, J. J. (1986). *The ecological approach to visual perception*. Hillsdale, New Jersey: Lawrence Erlbaum.

Giese, M. A., & Lappe, M. (2002). Measurement of generalization fields for the recognition of biological motion. *Vision Research, 42*(15), 1847–1858.

Graham, N. V. S. (1989). *Visual pattern analyzers*. New York: Oxford University Press.

Grill-Spector, K., Kushnir, T., Edelman, S., Itzchak, Y., & Malach, R. (1998). Cue-invariant activation in object-related areas of the human occipital lobe. *Neuron, 21*(1), 191–202.

Grill-Spector, K., Kushnir, T., Hendler, T., Edelman, S., Itzchak, Y., & Malach, R. (1998). A sequence of object-processing stages revealed by fMRI in the human occipital lobe. *Human Brain Mapping, 6*(4), 316–328.

Grossman, E., Donnelly, M., Price, R., Pickens, D., Morgan, V., Neighbor, G., et al. (2000). Brain areas involved in perception of biological motion. *Journal of Cognitive Neuroscience, 12*(5), 711–720.

Grossman, E. D., & Blake, R. (2002). Brain areas active during visual perception of biological motion. *Neuron, 35*(6), 1167–1175.

Grzywacz, N. M., Watamaniuk, S. N., & McKee, S. P. (1995). Temporal coherence theory for the detection and measurement of visual motion. *Vision Research, 35*(22), 3183–3203.

Habak, C., Wilkinson, F., Zakher, B., & Wilson, H. R. (2004). Curvature population coding for complex shapes in human vision. *Vision Research, 44*, 2815–2823.

Hayes, A. (2000). Apparent position governs contour-element binding by the visual system. *Proceedings of the Royal Society of London Series B: Biological Sciences, 267*(1450), 1341–1345.

Hildreth, E. C., Ando, H., Andersen, R. A., & Treue, S. (1995). Recovering three-dimensional structure from motion with surface reconstruction. *Vision Research, 35*(1), 117–137.

Johansson, G. (1973). Visual perception of biological motion and a model for its analysis. *Perception & Psychophysics, 14*, 201–211.

Kourtzi, Z., Bulthoff, H. H., Erb, M., & Grodd, W. (2002). Object-selective responses in the human motion area MT/MST. *Nature Neuroscience, 5*(1), 17–18.

Kourtzi, Z., & Kanwisher, N. (2001). Representation of perceived object shape by the human lateral occipital complex. *Science, 293*(5534), 1506–1509.

Ledgeway, T., & Hess, R. F. (2002). Rules for combining the outputs of local motion detectors to define simple contours. *Vision Research, 42*(5), 653–659.

Livingstone, M. S., & Hubel, D. H. (1987). Psychophysical evidence for separate channels for the perception of form, color, movement, and depth. *Journal of Neuroscience, 7*(11), 3416–3468.

Loffler, G., & Orbach, H. S. (2003). Factors affecting motion integration. *Journal of the Optical Society of America, A, Optics, Image Science, & Vision, 20*(8), 1461–1471.

Loffler, G., & Wilson, H. R. (2001). Detecting shape deformation of moving patterns. *Vision Research, 41*(8), 991–1006.

Loffler, G., Wilson, H. R., & Wilkinson, F. (2003). Local and global contributions to shape discrimination. *Vision Research, 43*(5), 519–530.

Lorenceau, J., & Alais, D. (2001). Form constraints in motion binding. *Nature Neuroscience, 4*(7), 745–751.

Lorenceau, J., & Zago, L. (1999). Cooperative and competitive spatial interactions in motion integration. *Visual Neuroscience, 16*(4), 755–770.

Maunsell, J. H., & van Essen, D. C. (1983). The connections of the middle temporal visual area (MT) and their relationship to a cortical hierarchy in the macaque monkey. *Journal of Neuroscience, 3*(12), 2563–2586.

Merigan, W. H., & Maunsell, J. H. R. (1993). How parallel are the primate visual pathways? *Annual Review of Neuroscience, 16*, 369–402.

Mukai, I., & Watanabe, T. (1999). The influence of structure from motion on motion correspondence. *Perception, 28*(3), 331–340.

Nakayama, K., He, Z. J., & Shimojo, S. (1995). Visual surface representation: A critical link between lower-level and higher-level vision. In S. M. Kosslyn & D. N. Osherson (Eds.), *Vision. An invitation to cognitive science* (pp. 1–70). Boston: MIT Press.

Neri, P., Morrone, M. C., & Burr, D. C. (1998). Seeing biological motion. *Nature, 395*(6705), 894–896.

Norman, J. F., & Lappin, J. S. (1992). The detection of surface curvatures defined by optical motion. *Perception & Psychophysics, 51*(4), 386–396.

Pasupathy, A., & Connor, C. E. (2002). Population coding of shape in area V4. *Nature Neuroscience, 5*(12), 1332–1338.

Pelli, D. G. (1997). The VideoToolbox software for visual psychophysics: Transforming numbers into movies. *Spatial Vision, 10*, 437–442.

Poirier, F., & Wilson, H. R. (2004). A neural model of radial frequency pattern perception. In *4th Annual meeting of the Vision Sciences Society* (p. 171). Sarasota, Florida: Journal of Vision.

Qian, N., Andersen, R. A., & Adelson, E. H. (1994). Transparent motion perception as detection of unbalanced motion signals. I. Psychophysics. *Journal of Neuroscience, 14*(12), 7357–7366.

Rainville, S., & Wilson, H. R. (2005). Closed-contour shapes encoded through deviations from circularity in lateral-occipital cortex: An fMRI study. In *5th Annual meeting of the Vision Sciences Society*. Sarasota, FL: Journal of Vision.

Rainville, S. J., Scott-Samuel, N. E., & Makous, W. L. (2002). The spatial properties of opponent-motion normalization. *Vision Research, 42*(14), 1727–1738.

Rainville, S. J., & Wilson, H. R. (2004). The influence of motion-defined form on the perception of spatially-defined form. *Vision Research, 44*(11), 1065–1077.

Sperling, G., & Landy, M. S. (1989). Kinetic depth effect and identification of shape. *Journal of Experimental Psychology: Human Perception & Performance, 15*(4), 826–840.

Tadin, D., Lappin, J. S., Blake, R., & Grossman, E. D. (2002). What constitutes an efficient reference frame for vision? *Nature Neuroscience, 5*(10), 1010–1015.

Tanaka, K. (1996). Inferotemporal cortex and object vision. *Annual Review of Neuroscience, 19*, 109–139.

Tanaka, K., & Saito, H. (1989). Analysis of motion of the visual field by direction, expansion/contraction, and rotation cells clustered in the dorsal part of the medial superior temporal area of the macaque monkey. *Journal of Neurophysiology, 62*(3), 626–641.

Todd, J. T. (1985). Perception of structure from motion: Is projective correspondence of moving elements a necessary condition? *Journal of Experimental Psychology: Human Perception & Performance, 11*(6), 689–710.

Ullman, S. (1979). The interpretation of structure from motion. *Proceedings of the Royal Society of London—Series B: Biological Sciences, 203*(1153), 405–426.

Ungerleider, L. G., & Desimone, R. (1982). Two cortical visual systems. In D. J. Ingle, M. A. Goodale, & R. J. W. Mansfield (Eds.), *Analysis of visual behavior* (pp. 549–580). Cambridge, MA: MIT Press.

Ungerleider, L. G., & Desimone, R. (1986). Cortical connections of visual area MT in the macaque. *Journal of Comparative Neurology, 248*(2), 190–222.

Vaina, L. M., Solomon, J., Chowdhury, S., Sinha, P., & Belliveau, J. W. (2001). Functional neuroanatomy of biological motion perception in humans. *Proceedings of the National Academy of Sciences of the United States of America, 98*(20), 11656–11661.

Van Essen, D. C., & Maunsell, J. H. (1983). Hierarchical organization and functional streams in the visual cortex. *Trends in Neurosciences, 6*, 370–375.

Van Essen, D. C., Maunsell, J. H., & Bixby, J. L. (1981). The middle temporal visual area in the macaque: Myeloarchitecture, connections, functional properties and topographic organization. *Journal of Comparative Neurology, 199*(3), 293–326.

Wallach, H., & O'Connell, D. N. (1953). The kinetic depth effect. *Journal of Experimental Psychology, 45*, 205–217.

Watanabe, T. (1997). Velocity decomposition and surface decomposition–reciprocal interactions between motion and form processing. *Vision Research, 37*(20), 2879–2889.

Wilkinson, F., James, T. W., Wilson, H. R., Gati, J. S., Menon, R. S., & Goodale, M. A. (2000). An fMRI study of the selective activation of human extrastriate form vision areas by radial and concentric gratings. *Current Biology, 10*(22), 1455–1458.

Wilkinson, F., Wilson, H. R., & Habak, C. (1998). Detection and recognition of radial frequency patterns. *Vision Research, 38*(22), 3555–3568.

Wilson, H. R., Ferrera, V. P., & Yo, C. (1992). A psychophysically motivated model for two-dimensional motion perception. *Visual Neuroscience, 9*(1), 79–97.

Wurtz, R. H., & Duffy, C. J. (1992). Neuronal correlates of optic flow stimulation. *Annals of the New York Academy of Sciences, 656*, 205–219.

Xiao, D. K., Raiguel, S., Marcar, V., & Orban, G. A. (1998). Influence of stimulus speed upon the antagonistic surrounds of area MT/V5 neurons. *Neuroreport, 9*(7), 1321–1326.

Young, M. P. (1992). Objective analysis of the topological organization of the primate cortical visual system. *Nature, 358*(6382), 152–155.

Yuille, A. L., & Grzywacz, N. M. (1988). A computational theory for the perception of coherent visual motion. *Nature, 333*(6168), 71–74.